The photodissociation dynamics of ozone at 193 nm: An $O(^1D_2)$ angular momentum polarization study

M. Brouard,[a] R. Cireasa,[b] A. P. Clark, G. C. Groenenboom,[c] G. Hancock, S. J. Horrocks, F. Quadrini, G. A. D. Ritchie, and C. Vallance
The Physical and Theoretical Chemistry Laboratory, The Department of Chemistry, University of Oxford, South Parks Road, Oxford OX1 3QZ, United Kingdom

(Received 13 April 2006; accepted 10 May 2006; published online 3 October 2006)

Polarized laser photolysis, coupled with resonantly enhanced multiphoton ionization detection of $O(^1D_2)$ and velocity-map ion imaging, has been used to investigate the photodissociation dynamics of ozone at 193 nm. The use of multiple pump and probe laser polarization geometries and probe transitions has enabled a comprehensive characterization of the angular momentum polarization of the $O(^1D_2)$ photofragments, in addition to providing high-resolution information about their speed and angular distributions. Images obtained at the probe laser wavelength of around 205 nm indicate dissociation primarily via the Hartley band, involving absorption to, and diabatic dissociation on, the $\tilde{B}\,^1B_2(3\,^1A_1)$ potential energy surface. Rather different $O(^1D_2)$ speed and electronic angular momentum spatial distributions are observed at 193 nm, suggesting that the dominant excitation at these photon energies is to a state of different symmetry from that giving rise to the Hartley band and also indicating the participation of at least one other state in the dissociation process. Evidence for a contribution from absorption into the tail of the Hartley band at 193 nm is also presented. A particularly surprising result is the observation of nonzero, albeit small values for all three rank $K=1$ orientation moments of the angular momentum distribution. The polarization results obtained at 193 and 205 nm, together with those observed previously at longer wavelengths, are interpreted using an analysis of the long range quadrupole-quadrupole interaction between the $O(^1D_2)$ and $O_2(^1\Delta_g)$ species. © *2006 American Institute of Physics*. [DOI: 10.1063/1.2210009]

I. INTRODUCTION

A. Atomic polarization studies

The electronic angular momentum polarization of the atomic fragments of molecular photodissociation has increasingly been a focus of attention over the past few years.[1–4] Its measurement involves the determination of the moments of the density matrix that characterizes fully the atomic product M_J populations and any coherences between different M_J states.[5,6] In many cases, the polarization of the electronic *orbital* angular momentum, **L** is the quantity of particular interest, and its characterization can help identify which of the possible exit channel potentials are involved in dissociation. This information is distinct from that provided by the angular distribution of the photofragments [described by the $\beta(v)$ parameter], which provides information principally about the symmetry of the electronic state(s) initially excited in the parent molecule. Knowledge of the electronic angular momentum orientation and alignment, coupled with more familiar information about populations and angular distributions, thus provides insight about changes in orbital populations or surface crossings during dissociation.

There has been very significant progress recently on the interpretation and theoretical calculation of orientation and alignment parameters.[7–9] In the case of photodissociation of diatomic molecules, the electronic angular momentum polarization gives information about excitation of multiple electronic states and nonadiabatic effects.[2,4,7–9] These processes can lead to interferences between wave packets evolving on different potential energy curves that correlate with the same asymptotic product states, and the polarization moments provide a very direct probe of these phenomena.[10] Although much of the theoretical work to date has been confined to diatomic molecules, extension to triatomic systems, albeit with more approximate methods, is by no means beyond the current scope. Simpler models that allow interpretation of electronic polarization information in more complex systems are also available.[8,11–14]

In the present work, the technique of velocity-map ion imaging is applied to a study of the molecular photodissociation of ozone at 193 and 205 nm, which has allowed determination of $O(^1D_2)$ electronic orbital angular momentum polarization moments up to and including those of rank $K=4$. Together with information about the velocity distribution of the $O(^1D_2)$ photofragments, we illustrate how the polarization data can be used to unravel the dissociation mechanism(s) operating in this important atmospheric molecule. Before we move on to describe the experimental and analytical procedures employed, we provide a brief résumé of previous work on ozone most relevant to the present study.

[a]Electronic mail: mark.brouard@chem.ox.ac.uk
[b]Permanent address: Laser Department, National Institute of Laser, Plasma and Radiation Physics, P.O. Box MG-36, Bucharest, Romania.
[c]Institute of Theoretical Chemistry, IMM, Radboud University Nijmegen, Toernooiveld 1, 6525 ED Nijmegen, The Netherlands.

B. Previous relevant work on ozone at 193 nm and other wavelengths

Ozone photochemistry has been the subject of extensive experimental and theoretical study due to its atmospheric importance and complex dissociation dynamics. The uv absorption spectrum of ozone[15] is dominated by the intense Hartley band, which results in stratospheric O_3 acting as a highly efficient filter of solar radiation in the wavelength range of 220–310 nm. At lower energies, the Hartley band is partially overlapped by the much weaker Huggins band.[15] On the short wavelength side of the Hartley band, the absorption cross section shows a minimum at 201 nm (3.1×10^{-19} cm^2) and then increases again with shortening wavelength, indicating the onset of a new absorption feature.[15,16] This short wavelength region has been rarely investigated due to the unfavorable absorption cross sections, and also because the solar flux at wavelengths around 193 nm is low enough that dissociation in this region was considered unimportant. However, around 190 nm, gaps in the Schumann-Runge bands of oxygen allow light to penetrate into the upper and middle stratosphere, and so ozone photolysis in this region, producing $O(^1D_2)$, remains of significance.

There are a total of six spin-allowed, energetically accessible product channels open in the photodissociation of ozone at 193 nm.[16] Detailed product quantum yields for all of the accessible channels have not yet been determined, although Turnipseed *et al.*[17] reported $\phi[O(^1D_2)] = 0.46 \pm 0.29$ and $\phi[O(^3P_J)] = 0.57 \pm 0.14$. The fact that the sum of the quantum yields is greater than unity was ascribed to the operation of a dissociation channel producing three $O(^3P_J)$ atoms. A quantum yield for $O_2(b\ ^1\Sigma_g^+)$ of 0.50 ± 0.38 was also measured, and it was concluded that $O(^1D_2)$ and $O_2(b\ ^1\Sigma_g^+)$ were generated as coproducts. These results are in good agreement with the findings of a vacuum ultraviolet (vuv) laser induced fluorescence (LIF) experiment by Takahashi *et al.*[18] and Nishida *et al.*,[19] who measured $\phi[O(^1D_2)] = 0.48 \pm 0.03$. A high-resolution photofragment translational spectroscopy study carried out by Stranges *et al.*[20] also allowed estimates to be made of the branching ratios for several of the energetically open channels; most notable in the context of the present work are those into the channels $O(^1D_2)+O_2(a\ ^1\Delta_g)$ and $O(^1D_2)+O_2(b\ ^1\Sigma_g^+)$ (see Sec. III). Note that the former channel is dominant [$\phi \sim 0.9$ (Ref. 16)] following excitation into the peak of the Hartley band. Evidence was also found for the three-atom dissociation channel. Recently, Takahashi *et al.*[21] detected the $O(^1S)$ atoms from ozone photolysis at 193 nm, again using the vuv-LIF technique, and determined a quantum yield of 2.5×10^{-3}.

Compared with the Hartley band,[22–25] rather little attention has been paid to the photodissociation dynamics following 193 nm excitation. In the photofragment translational spectroscopy study of Stranges *et al.*,[20] both the speed distribution and translational anisotropy of the recoiling O-atom fragments were determined, with the latter found to be opposite in sign to that observed subsequent to excitation into the Hartley band.[22] These measurements were corroborated by the vuv-LIF experiments of Takahashi *et al.*,[18] who obtained low-resolution speed and translational anisotropy parameters for both $O(^1D_2)$ and $O(^3P)$ photofragments separately from Doppler-resolved LIF measurements.

In addition to the above-mentioned work, a number of $O(^1D_2)$ atomic polarization studies at longer wavelengths are deserving of special mention. The first of these is the important angular momentum alignment study performed by Dylewski *et al.*[22] They observed preferential population of $M_L = 1$ levels at selected wavelengths across the Hartley band between 235 and 305 nm but also found evidence for contributions from coherence terms.[22] The M_L population results were interpreted as being consistent with dissociation on a state of A' symmetry.[22] More recently, Lee *et al.*[23] carried out an elegant slice imaging study of ozone photofragmentation via the Hartley band, in which they observed strong, speed-dependent $O(^1D_2)$ orientation following absorption of plane polarized light. The origin of this orientation was ascribed principally to a "static" coherence effect, arising from coherent excitation of both parallel and perpendicular (in plane) components of the transition moment with respect to the recoil direction of the atom. It was argued[23] that this coherence could persist, or be quenched, by nonadiabatic transitions at avoided crossings or in the long range region and could also be influenced by long range O–O–O bond angle dependent effects, similar to those described in the case of the photodissociation of N_2O Ref. 11 and SO_2.[13] Finally, very recently Denzer *et al.*[25] have published an in-depth resonantly enhanced multiphoton ionization (REMPI) time-of-flight study of the $O(^1D_2)$ atomic orbital polarization generated by photofragmentation in the long wavelength region of the Hartley band at 298 nm. They were able to determine moments of the angular momentum distribution of rank up to $K=4$, including $K=1$ orientation moments. Their results were in general agreement with those of both Dylewski *et al.*[22] and Lee *et al.*[23] However, compared with the former work, Denzer *et al.*[25] observed a small coherence term, and it was suggested that this reflected the nuclear geometry of the dissociating molecule and the existence of possible nonadiabatic effects in the exit channel. Of particular note in the present context, and in agreement with the study by Lee *et al.*,[23] Denzer *et al.*,[25] found that of the three possible $K=1$ orientation moments, only that arising from the static coherence mechanism (γ_1') was nonzero. We return to a discussion of this point in Sec. IV E.

II. METHOD

A. Experimental procedures

The experiments were carried out using a standard velocity-map[26] ion imaging[27] apparatus that has been described in detail previously.[12,13,28–30] 15% of an ~1:1 O_3/O_2 mixture, prepared using a commercial ozonizer, was seeded in He at a backing pressure of ~1 bar and expanded through a pulsed nozzle (General Valve) with a 0.5 mm diameter orifice. The molecular beam was collimated by a 1 mm diameter skimmer. The rotational temperature of the skimmed molecular beam was believed from our previous work on the same apparatus to be ~50 K. Further downstream, the molecular beam was passed through a 2 mm hole in the repeller

plate of the velocity mapping ion optics assembly and crossed 5 cm away from the nozzle exit by two counterpropagating laser beams. The 193 nm photolysis radiation was provided by a Lambda Physik EMG103 excimer laser, while the probe radiation, operating typically at pulse energies of around 500 μJ pulse^{-1}, was obtained by frequency doubling the output of a Nd:YAG (yttrium aluminum garnet)-pumped dye laser system (Photonic Solutions). The time delay between the two laser pulses was ~10 ns. Two lenses of 30 cm focal length were used to focus the radiation onto the molecular beam.

The O($^1D_2$) photofragments were probed by (2+1) resonantly enhanced multiphoton ionization (REMPI) via the $^1F_3 \leftarrow {}^1D_2$ and $^1P_1 \leftarrow {}^1D_2$ (labeled in the following as the $F\uparrow$ and $P\uparrow$) transitions at 203.8 and 205.4 nm, respectively.[31] During image acquisition, the probe laser wavelength was scanned over the Doppler profile of the O($^1D_2$) transitions in order to ensure an equal detection sensitivity for all the product velocities. The oxygen ions were velocity mapped onto an imaging detector consisting of a pair of 40 mm chevron double microchannel plates (MCPs) coupled to a P47 phosphor screen (DelMar Ventures). The image on the phosphor screen was captured by an intensified charge coupled device (CCD) camera (Photonic Science), electronically gated to the flight time of the detected ions, and subsequently sent to a personal computer (PC) for signal processing (thresholding, event counting,[32] and accumulation). Images were averaged over 25 000 laser shots. Velocity calibration of the final images was achieved using images of O(^3P_J) from the photodissociation of O_2, the energetics for which is well characterized.[33]

In order to extract information on the O($^1D_2$) atom polarization, images were obtained for both O-atom transitions in a variety of pump-probe laser geometries. These included the more usual geometries used previously to extract alignment parameters and labeled HH, HV, VH, and VV according to the polarization of the pump and probe lasers lying parallel (H) or perpendicular (V) to the image plane. As with most conventional ion-imaging machines, note that the molecular beam axis is perpendicular to the image plane. Data were also collected in other configurations, including both linearly (with the electric vector of the light at ±45° to the time-of-flight axis) and left (L) and right (R) circularly polarized photolysis radiation. The use of such a large number of geometries, together with two probe transitions, helped ensure that the moments of the angular momentum distribution could be obtained unambiguously. Pairs of images were collected simultaneously by using a photoelastic modulator to switch the probe laser polarization on alternate laser shots. This procedure not only reduced the errors due to drift during an experiment but also enabled the measurement of the total angular momentum orientation, $\langle A_{10} \rangle$, and alignment, $\langle A_{20} \rangle$, from the measured intensity ratios.[4] These parameters are required in order to normalize the image intensities (see further discussion in Sec. II B). Circularly polarized probe laser radiation was generated using a photoelastic modulator, and in this case, geometries were switched from L to R circular polarization on alternating laser shots. Note that in switching from L to R probing, only the sensitivity to the odd polarization moments (orientation) is changed.

Finally, images were also recorded on alternate pairs of shots with and without firing the photolysis laser. This procedure allowed the total signal and "probe-only" ion images to be accumulated concurrently and subsequently subtracted if necessary to remove background signal arising from ions formed through processes involving only the probe laser wavelength.

B. Data analysis

The analysis of angular momentum polarization effects on ion images was previously achieved by fitting basis functions, generated in terms of a semiclassical bipolar moment formalism,[1] to Fourier moments of the ion images.[28] In the present work, we proceed along similar lines but start from the quantum mechanical expression for the O-atom REMPI signal intensity in pump-probe geometry j given by Suits and co-workers,[4,23,34,35] adapted for multiple velocities,

$$I(\Theta,\Phi;v) = C\sum_{KQ} P_K \rho_{KQ}(\Theta,\Phi;v) C^*_{KQ}(\Theta^j_a,\Phi^j_a). \tag{1}$$

In this equation C is a normalization constant, P_K are line strength factors for the REMPI transition,[35,36] $C_{KQ}(\cdots)$ is a modified spherical harmonic, and (Θ^j_a,Φ^j_a) define the direction of the probe (analysis) laser reference vector in the laboratory frame (see Sec. IV A). The latter is defined such that the Z axis lies parallel to the time-of-flight (TOF) axis and the X axis lies along the propagation direction of the photolysis laser. The $\rho_{KQ}(\Theta,\Phi;v)$ are speed- (and geometry j) dependent elements of the density matrix for the angular momentum distribution,[5] or the angular momentum state multipoles of rank K and component Q at some laboratory frame scattering angle defined by (Θ,Φ). The moments have been defined by Siebbeles *et al.*[2] and subsequently modified for application to ion imaging as:[4,7,35]

$$\begin{aligned}\rho_{KQ}(\Theta,\Phi;v) = \frac{3}{4\pi}\left(\frac{[K]}{[j_A]}\right)^{1/2} \sum_{k_d,q_d,Q'} \sum_{q,q'} (-1)^{K+q'} \\ \times E_{k_d q_d}(\mathbf{e}_j)[k_d]^{1/2} f'_K(q,q';v) \\ \times \begin{pmatrix} 1 & 1 & k_d \\ q' & -q & -Q' \end{pmatrix} \\ \times D^{K^*}_{QQ'}(\Phi,\Theta,0) D^{k_d}_{q_d Q'}(\Phi,\Theta,0).\end{aligned} \tag{2}$$

In this equation, $[i]=2i+1$, the terms in large brackets are 3-J symbols, the $D(\cdots)$ are Wigner rotation matrices, and $Q'=q'-q$. j_A is the angular momentum of the probed atom, which in the case of O($^1D_2$) is equivalent to L. $E_{k_d q_d}(\cdots)$ are the matrix elements of the polarization tensor of the photodissociation light for geometry j and rank k_d (Ref. 5) and are defined as[4,35,37]

$$E_{k_d q_d}(\mathbf{e}_j) = (-1)^s [k_d]^{1/2} \begin{pmatrix} 1 & 1 & k_d \\ s & -s & 0 \end{pmatrix} C_{k_d q_d}(\Theta_d^j, \Phi_d^j), \quad (3)$$

where the angles (Θ_d^j, Φ_d^j) define the direction of the reference vector of the photolysis radiation in the laboratory frame (see Sec. IV A).

The $f'_K(q,q';v)$ terms in Eq. (2) are renormalized speed-dependent dynamical functions that contain the polarization information of interest for the system.[2] The renormalized dynamical functions are defined here as[2,4]

$$f'_K(q,q';v) = \frac{f_K(q,q';v)}{\langle f_0(0,0;v)\rangle + 2\langle f_0(1,1;v)\rangle},$$

where $\langle f_K(q,q';v)\rangle$ represent the integral of the dynamical functions over recoil speed. In the present work, the speed dependence of the dynamical parameters is expressed as a linear combination of Gaussian functions:

$$f'_K(q,q';v) = N \sum_i a_K(q,q';i) e^{-\sigma(v_i - v)^2}, \quad (4)$$

where N is a normalization constant, $a_K(q,q';i)$ are Gaussian specific polarization parameters, σ is a width parameter, and v_i are the Gaussian centers. In practice, the $f'_K(q,q';v)$ dynamical factors are usually recast in a variety of different (but parametrically equivalent) ways, including the polarization parameters of Rakitzis and Zare[3] and the polarization anisotropy parameters of Vasyutinskii and co-workers.[4,23,35,38] In the present work we use the latter set of parameters.

By contracting the product of rotation matrices in Eq. (2) and then integrating over the laboratory frame Z axis, the ion-image intensity can be expressed in the form of a Fourier series,

$$I(r,\Phi) = \Re\{c_0(r)\} + \sum_{n>0} \Re\{c_{n+}(r)\}\cos n\Phi - \Im\{c_{n-}(r)\}\sin n\Phi, \quad (5)$$

with the simulated, geometry-specific Fourier moments c_n of the image being dependent on the $a_K(q,q';i)$ parameters:

$$c_{n\pm}(r) = \sum_{i=1} \sum_{K,q,q'} a_K(q,q';i) G(K,q,q',i,n\pm,j;r).$$

$G(K,q,q',i,n,j;r)$ represent a basis set for the simulated moments specific to the experimental geometry employed. Explicitly, they can be written as

$$G(K,q,q',i,n\pm,j;r) = C \sum_{Q=-K}^{K} P_K \rho_{KQ}(q,q',i,n\pm,j;r) C^*_{KQ}(\Theta_a^j, \Phi_a^j),$$

with

$$\rho_{KQ}(q,q',i,n\pm,j;r) = [\rho_{KQ}(q,q',i,+n,j;r) \pm \rho_{KQ}(q,q',i,-n,j;r)]$$

and

$$\rho_{KQ}(q,q',i,n,j;r) = \frac{3}{4\pi}\left(\frac{[K]}{[j_A]}\right)^{1/2} \sum_{k_d} (-1)^{K+q+Q} \times E_{k_d q_d}(\mathbf{e}_j)[k_d]^{1/2} \begin{pmatrix} 1 & 1 & k_d \\ q' & -q & -Q' \end{pmatrix} \times \sum_{K'} [K'] \begin{pmatrix} K & k_d & K' \\ -Q & q_d & n \end{pmatrix} \begin{pmatrix} K & k_d & K' \\ -Q' & Q' & 0 \end{pmatrix} \times [1 + (-1)^{K'+n}] \int N e^{-\sigma(v_i - v)^2} \times C_{K'n}(\Theta, 0) dv_Z.$$

The experimentally acquired images can also be cast in a form analogous to Eq. (5) by performing a Fourier integral:

$$\mathcal{I}(r,\Phi) = C_0(r) + 2\sum_{n>0} C_n(r)\cos n\Phi + C'_n(r)\sin n\Phi. \quad (6)$$

In fitting the simulated Fourier moments of the images to the experimental data, the quality of the fit (χ^2) was calculated by directly comparing experimental and fitted Fourier moments of equivalent order n. In this work, the fitted parameters $a_K(q,q';i)$ for a given number of Gaussians, $i_{\max}=25$, were selected using a genetic algorithm from a pool of parameters randomly generated within the constraints of the physically allowed values. A Monte Carlo procedure, described fully elsewhere,[28] was then used to determine the errors on the fitted coefficients and on the speed-dependent moments of the angular distribution.

To reduce the number of fitting coefficients, the speed dependence of the polarization parameters was described in terms of a Legendre polynomial expansion. The fitted coefficients for all polarization parameters [excluding those for the speed distribution, characterized by the set of coefficients $a_0(i) \equiv a_0(0,0;i) + 2a_0(1,1;i)$] were expressed as a convolution of the speed distribution parameters and a Legendre polynomial $[P_l(\cdots)]$ series with nleg, the maximum order, set to 3:

$$a_K(q,q';i) = a_0(i) \sum_{l=0}^{\text{nleg}} b_K(q,q';l) P_l(x_i), \quad (7)$$

where

$$x_i = 2\frac{i-1}{i_{\max}-1} - 1. \quad (8)$$

This procedure allowed for the speed dependence of the polarization parameters while significantly reducing the basis set size.

Correct analysis of the ion images requires careful renormalization of the raw data, taking into account the integrated (over speed) angular momentum orientation and alignment. In the fitting procedure used in the present work, renormalization was done on the fly using the expressions for the integrated image intensity given in Appendix A.

In the case of diatomic molecules, the dynamical functions have been interpreted in terms of contributions to the

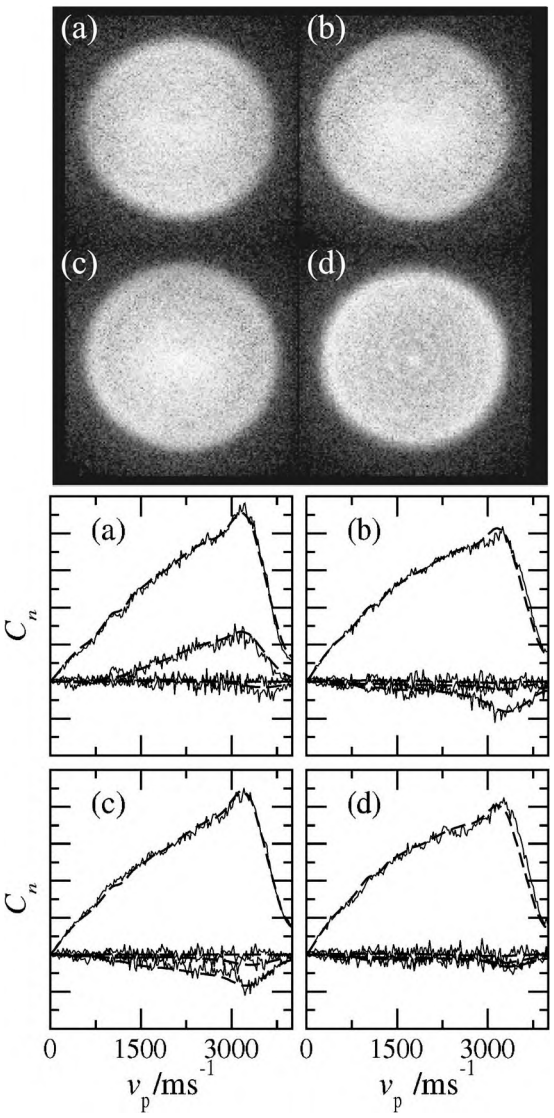

FIG. 1. Representative velocity-map ion images (top four panels) and their Fourier moments (lower four panels) for the $O(^1D_2)$ fragments generated subsequent to photodissociation of O_3 at 193 nm. The fits to the Fourier moments are shown as dashed lines (see text for details). The four sets of images and the corresponding moments employ (a) the $^1F_3 \leftarrow {}^1D_2$ REMPI transition with LR circularly polarized pump and probe light, (b) the $^1P_1 \leftarrow {}^1D_2$ transition and RL polarized light, (c) the $^1P_1 \leftarrow {}^1D_2$ transition and VL polarized light, and (d) the $^1P_1 \leftarrow {}^1D_2$ transition and +45° L polarized light. See text for notation.

dynamics by transitions to the dissociation continuum with their transition dipole moment vectors lying either parallel $(q,q'=0)$ or perpendicular $(q,q'=\pm 1)$ to the bond axis. Interpretation of the polarization parameters in the case of larger systems,[23,39] is more problematic and awaits a detailed theoretical treatment. In the present work we have used the polarization parameters to calculate the electron hole distribution of the atomic photofragment, representing the polarization of the electron hole, and the atomic product quantum mechanical angular momentum distribution, which represents the polarization of the electronic orbital angular momentum **L**. These quantities provide a useful and rigorous means of interpreting the polarization parameters, which remain valid even for polyatomic systems such as ozone. The distributions can be calculated from a knowledge of the molecular frame state multipoles, $\rho_{KQ}^{\mathrm{mol}}(\theta,\phi;v)$, using the equations developed from those by Brouard *et al.*[12] and de Miranda and co-workers.[40,41] Equations for $\rho_{KQ}^{\mathrm{mol}}(\theta,\phi;v)$ are given in Appendix B. In the following, the molecular frame moments are integrated over the recoil speed, and these integrated moments will be referred to as the $\rho_{KQ}^{\mathrm{mol}} \equiv \langle \rho_{KQ}^{\mathrm{mol}}(\theta,\phi;v) \rangle$ molecular frame moments.

III. RESULTS

A. Images, moments, and fits

Representative ion images, their Fourier moments and the fits to those moments are shown in Fig. 1. For the pump-probe data at 193 nm, simultaneous fits were performed on 28 separate ion images, obtained using either different pump-probe geometries or different REMPI probe transitions. Of particular significance to the present work is the fact that these data also included the moments of ion images obtained in geometries sensitive to orientation (see further below). The probe-only data, obtained with just the REMPI laser firing at wavelengths around 205 nm, were also analyzed. These data were not sensitive to orientation moments of the angular momentum distribution but, in principle, could be used to determine angular momentum alignment. However, it proved impossible to obtain enough independent probe-only geometries to allow successful extraction of all of the polarization parameters, and thus, a reduced set was determined by setting all $K=4$ moments to zero. This is a reasonable first approximation since these higher moments tend to have less influence on the image data than the low-order moments, particularly for the $F\uparrow$ transitions which have smaller $K=4$ line strength factors (i.e., $P_4 < P_2$). The reduced set of probe-only geometries (HH, VV, LL, and RR) was also found to be insensitive to the γ_2 alignment parameter, and equally good fits could be obtained when this parameter was set to zero. It should be emphasized that in spite of these uncertainties, the returned speed distribution and speed-dependent $\beta(v)$ parameter obtained from the analysis were found to be fairly insensitive to the number of moments used in the analysis.

B. Speed distributions and $\beta(v)$

The speed distributions obtained at 193 and 205 nm, together with the associated speed-dependent translational anisotropy parameters $\beta(v)$, are presented in Fig. 2. Although the speed distributions at the two wavelengths are similar, that obtained at the shorter wavelength shows increased intensity at low translational energies, and there is a hint of bimodality in the distribution that is completely absent at 205 nm, possibly indicative of the emergence of a second dissociation channel. As shown by the comparison in Fig. 2(b), the 205 nm data are in excellent agreement with the speed distribution obtained in the recent quantum mechanical (QM) study of the dissociation dynamics by Baloitcha and Balint-Kurti following excitation into the short wavelength region of the Hartley band.[42,43] The comparison lends support to the notion that, notwithstanding the slight reduction in $\beta(v)$ parameter (see below), even at wavelengths as short

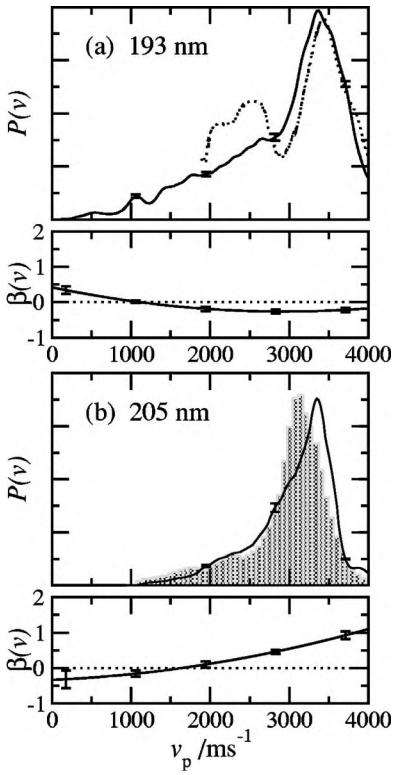

FIG. 2. Speed distributions and $\beta(v)$ parameters obtained at (a) 193 nm and (b) 205 nm. In (a) the dotted line corresponds to that portion of the O-atom speed distribution observed by Stranges *et al.* assigned by them to $O(^1D)$ atom production (Ref. 20). In (b) the experimental data are compared with the QM calculations of Baloitcha Balint-Kurti (Ref. 43), which are shown as the shaded data. The latter were performed for excitation into the blue end of the Hartley band and employed the calculated $\tilde{B}(3\,^1A')$ state potential, by the same authors (Ref. 42).

as 205 nm, the dominant pathway to formation of $O(^1D_2)$ photofragments remains dissociation on the diabatic $\tilde{B}$-state potential energy surface (PES).

The speed and translational anisotropy distributions obtained in the present work are in reasonable agreement with those measured by Stranges *et al.*[20] using the molecular beam, time-of-flight mass spectrometry technique [see Fig. 2(a)], although the results from the latter study show somewhat more pronounced structure. It is worth noting, however, that the previous experiments were insensitive to the electronic state of the atomic oxygen. In the kinetic energy region of interest, Stranges *et al.*[20] tentatively associated the bimodality in the speed distribution to production of O_2 in two electronically excited states: the $a\,^1\Delta_g$ state (with a quantum yield of 48%), which is the dominant coproduct subsequent to excitation into the peak of the Hartley band,[16] and the $b\,^1\Sigma_g^+$ state (with a quantum yield of 23%). A very crude integration of the speed distribution obtained here at 193 nm into fast ($v > 3000$ m s^{-1}) and slow ($v < 3000$ m s^{-1}) components yields branching fractions of 0.59 (fast) and 0.41 (slow), similar to those reported by Stranges *et al.*[20] Although the speed distribution obtained in the present work is insufficiently structured to allow definitive identification of the electronic state of the O_2 cofragment, independent (albeit indirect) evidence for production of $O_2(b\,^1\Sigma_g^+)$ at 193 nm has been provided by Turnipseed *et al.*[17] Interestingly, their measurements,[17] which involved the observation of the slow production of $O(^3P)$ from reaction of $O_2(b\,^1\Sigma_g^+)$ with O_2, suggested production of $O_2(b\,^1\Sigma_g^+)$ at 193 nm, but *not* at 205 nm, consistent with the different forms for the speed distributions observed here at the two wavelengths. Finally, with respect to the molecular beam study by Stranges *et al.*,[20] it should be mentioned that the present measurements seem to rule out assignment of the two peaks they observed in the translational energy release distribution at low kinetic energies (labeled 5 and 6 in Ref. 20) to channels involving $O(^1D)$ production.

TABLE I. Speed-integrated angular momentum polarization parameters for $O(^1D_2)$ products of O_3 photodissociation at 193 nm. Numbers in parentheses give the 2σ experimental errors in the final decimal place(s). The final two columns refer to the same moments broken down into contributions from slow (<3000 m s^{-1}) and fast (>3000 m s^{-1}) $O(^1D_2)$ photofragments, which contribute 41% and 59%, respectively, to the total product signal.

Polarization parameter	This study	Slow	Fast
β	−0.213(34)	−0.188	−0.230
α_1	−0.014(9)	−0.005	−0.020
γ_1	0.031(20)	−0.003	0.055
γ_1'	−0.018(17)	−0.039	−0.004
s_2	−0.071(6)	−0.074	−0.068
α_2	−0.007(4)	−0.023	0.005
γ_2	−0.019(9)	0.006	−0.035
η_2	0.013(7)	−0.018	0.035
s_4	0.056(17)	0.029	0.075
α_4	−0.005(6)	0.021	−0.022
γ_4	0.002(24)	0.089	−0.057
η_4	−0.005(17)	0.012	−0.016

The speed and spatial anisotropy data obtained at 193 nm are also in excellent agreement with the low-resolution Doppler resolved LIF measurements of Takahashi *et al.*[18] Note that excitation of ozone at 193 nm yields a negative translational anisotropy (with a speed-integrated value of −0.21, as shown in Table I), whereas excitation into the peak of the Hartley band yields a positive β parameter, greater than unity.[18,22] The β parameter obtained at probe-only wavelengths around 205 nm (+0.59) is significantly smaller than the value associated with absorption into the peak of the Hartley band, although unlike the value obtained at 193 nm it has the same sign. The reduced β parameter at 205 nm, compared with that obtained, for example, at 255 nm (where it is 1.29),[22] might be taken as evidence for an increasing contribution from a perpendicular transition with decreasing wavelength. However, in the light of the excellent agreement between the photofragment speed distribution obtained here and the QM calculations of Baloitcha and Balint-Kurti,[42,43] which include only the diabatic $\tilde{B}$-state potential, it seems possible that the reduction in β at 205 nm might be associated with other factors, such as a change in the direction of the transition moment with geometry or an increase in the $O_2(a\,^1\Delta_g)$ rotational excitation at shorter wavelengths. The recent *ab initio* calculations of the transition moment carried out by Baloitcha and Balint-Kurti[42] certainly support the former notion, with the ratio of the two in-plane components of the transition dipole moment chang-

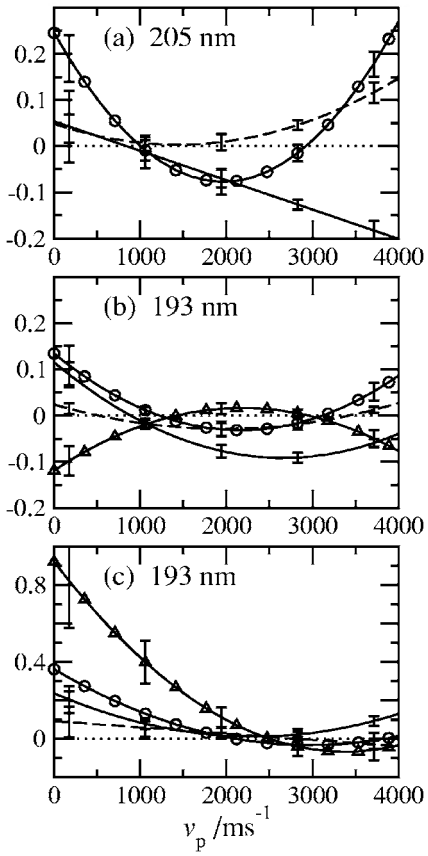

FIG. 3. O($^1D_2$) alignment polarization moments for (a) rank $K=2$ obtained at 205 nm, (b) rank $K=2$ at 193 nm, and (c) rank $K=4$ at 193 nm. The symbols employed, which are not to be confused with individual data points, are as follows: s_k —, α_k ---, γ_k -△-, and η_k -○-. Note that γ_2 was not determined at 205 nm. The dotted line marks zero on the plots.

ing significantly with compression or extension of one of the O–O bonds away from C_{2v} configurations. Indeed, contributions to the Franck-Condon region accessed at 193 nm from configurations with reduced O–O bond extensions of only a few tenths of a bohr, which seems reasonable based on the energetics and the published PESs,[42–45] could significantly reduce β from the value observed at the maximum in the Hartley band.

To summarize the above evidence, it would appear that at 205 nm the predominant absorption is into the Hartley band, leading to similar photodissociation dynamics to that previously observed at longer wavelengths.[18,22] In contrast, excitation at 193 nm appears to involve predominantly a transition to a state of either $^1A_1(^1A')$ or $^1B_1(^1A'')$ symmetry, both of which could be associated with negative translation anisotropy parameters. The velocity distribution of the O atoms at this wavelength provides supporting evidence for the operation of two dissociation pathways[17,20] leading to O_2 molecular cofragments born in either the a or the b states. These two pathways could either reflect photon absorption via a mixed transition or curve crossings along the dissociation pathway. The similarity of the high speed component of the O($^1D_2$) speed distribution with that predicted and observed for the Hartley band suggests that some contribution from excitation into the tail of the Hartley band should not be ruled out, even down to wavelengths as low as 193 nm.

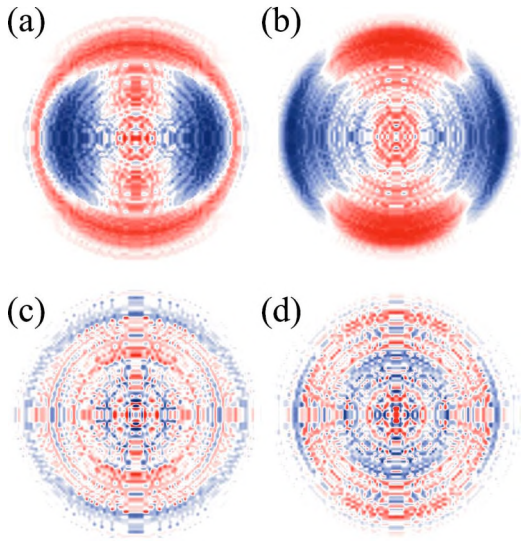

FIG. 4. (Color online) Difference images for R-L circularly polarized light obtained at 193 nm. Top row: $^1P_1 \leftarrow {}^1D_2$ REMPI data for (a) circularly polarized (R) photolysis and for (b) linearly polarized photolysis at 45° to the time of flight axis. Bottom row: (c) and (d), as for (a) and (b) but using $^1F_3 \leftarrow {}^1D_2$ REMPI transition. The upper panels are sensitive to moments with $K=1$, while the lower panels are sensitive to moments with $K=3$.

C. Polarization parameters

The speed dependences of the alignment parameters with $K=2$ and 4 are presented in Figs. 3(a)–3(c). Like the $\beta(v)$ parameters shown in Fig. 2, the polarization parameters have been normalized to the speed distribution. For this reason the values of the parameters below 1000 m s^{-1} and in excess of 4000 m s^{-1} (not shown in the figures) should be treated with caution, since very few fragments are born with speeds outside these limits. The data obtained at 193 nm were sufficient for moments with $K=4$ also to be determined. Although the contribution of these higher-order moments to the signal is small, the quality of the fits was improved significantly by their inclusion in the analysis, particularly in respect of the $P\uparrow$ versus the $F\uparrow$ transitions. In practice, only one of the fourth-order moments s_4 makes a large contribution to the data, as shown more clearly once the parameters are integrated over speed (see below).

In the case of the orientation moments, data were recorded using $P\uparrow$ and $F\uparrow$ REMPI transitions, employing both linearly and circularly polarized photolysis radiation. Difference images, obtained after subtraction of images obtained on alternate laser shots using left and right circularly polarized *probe* light, are shown in Fig. 4. While the difference data for the $P\uparrow$ data show a clear orientation signal, those for the $F\uparrow$ transition are too small to be observed within the signal-to-noise ratio of the experiment. The line strength factors for the two transitions, i.e., the P_K term in Eq. (1), are very different, with the difference signal for the $P\uparrow$ transition being sensitive only to the odd orientation moments with $K=1$ and the $F\uparrow$ transition exclusively sensitive to the $K=3$ moments of the distribution. Thus, the difference images shown in Fig. 4 provide direct evidence that the $K=1$ moments of the distribution are significant, while the $K=3$ moments are considerably smaller and cannot be determined. The speed-dependent laboratory frame orientation param-

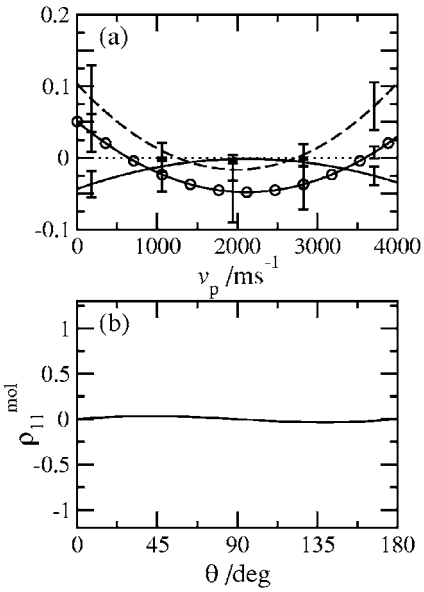

FIG. 5. (a) As for Fig. 3, but showing the laboratory frame $K=1$ orientation moments obtained at 193 nm, with the notation α_1 —, γ_1 ---, and γ_1' -○-. (b) the experimentally derived molecular frame moment $\Im[\rho_{11}]$ arising from photodissociation with linearly polarized light at 193 nm.

eters returned by the Fourier-moment analysis are shown in Fig. 5(a). A particularly interesting feature, discussed further in Sec. IV E, is that nonzero values are obtained for all three $K=1$ moments.

The speed-integrated polarization parameters are listed in Tables I and II. In the final two columns of Table I, which summarizes the data obtained at 193 nm, the polarization parameters are resolved into fast ($v>3000$ m s^{-1}) and slow ($v<3000$ m s^{-1}) components. This was achieved by separate integration over the two speed components, followed by renormalization according to their relative probabilities. Some of the moments change sign between the two speed regimes, while others differ in magnitude between the two components, and in a more complete analysis one might explore the polarization of the two speed components separately. However, it is evident from the data in Table I that the speed-*integrated* moments are generally dominated by the contribution from the major, high speed component. Thus in the present work we focus only on the speed-integrated moments, which tend to reflect the behavior of the fast $O(^1D_2)$ photofragments. Table II includes a comparison between the polarization moments obtained in the present work at 193 and 205 nm with those derived in the previous work by Dylewski *et al.* at 255 nm.[22] Bearing in mind the difficulties noted in Sec. II B concerning the analysis of the probe-only data, there is broad agreement between the data sets at 205 and 255 nm.[22] This agreement gives strength to the argument that photodissociation at 205 nm occurs predominately via the diabatic $\tilde{B}$ state. Note, on the other hand, that at 193 nm, where a different transition clearly dominates, the $K=2$ polarization moments are significantly reduced in magnitude compared with those observed in the previous work of Dylewski *et al.* at 255 nm.[22]

TABLE II. Comparison of the speed-integrated angular momentum alignment parameters for the $O(^1D_2)$ products of O_3 photodissociation at 193 nm with the present results at 205 nm and the previous work at 255 nm by Dylewski *et al.* (Ref. 22). For comparison with the present work, the latter has been averaged over O-atom speed. Numbers in parentheses give the (2σ) experimental error in the final significant figures. Here we employ the notation of Rakitzis and Zare (Ref. 3), as defined by Alexander (Ref. 39).

Alignment parameter	This study at 193 nm	This study at 205 nm	Dylewski *et al.* at 255 nm
β	−0.21(3)	0.59(10)	1.29
$a_{20}(\parallel)$	−0.36(6)	−0.86(7)	−0.84
$a_{20}(\perp)$	−0.35(3)	−0.53(10)	−0.35
$a_{21+}(\parallel,\perp)$	−0.17(8)	0.00(80)	−0.23
$a_{22+}(\perp,\perp)$	−0.05(3)	−0.27(7)	−0.08

IV. DISCUSSION

A. Electron density and angular momentum distributions

As was noted in Sec. II B, further interpretation of the polarization parameters requires transformation into the molecular frame. Following previous work,[4] the latter is defined with the z axis lying along the recoil direction and the zx plane containing the reference axis of the photolysis radiation, taken to be either the polarization (for linearly polarized light) or propagation (for circularly polarized light) direction of the photolysis radiation. The transformation of the polarization parameters is a generalization of that described by Bracker *et al.*[4] and is given in Appendix B. In the following, we focus exclusively on the data obtained using linearly polarized photolysis and return to the issue of circularly polarized photodissociation in Sec. IV E. For the reasons discussed in Sec. III, we also concentrate on the speed-integrated behavior. The single molecular frame moment for $K=1$ obtained using linearly polarized photolysis at 193 nm is shown in Fig. 5(b), while the even-moment data obtained at 193 and 205 nm are shown in Fig. 6. In these figures the moments are plotted as functions of recoil angle θ, which represents the angle between the recoil velocity and the reference axis of the photolysis radiation.[4] Figure 6 also includes the molecular frame moments derived from the polarization parameters measured by Dylewski *et al.* at 255 nm.[22] The $K=2$ moments are dominated by the ρ_{20}^{mol} parameter, which is negative in sign, although at 205 and 255 nm this moment is reduced somewhat in magnitude for scattering angles centered around 90°. These results are consistent with the predominant population of low M_L states, and $M_L=0$ for $\theta\sim0°$ and 180°, i.e., **L** alignment is preferentially perpendicular to the recoil direction, as noted previously by Dylewski *et al.* for excitation into the Hartley band.[22] In contrast with this, the magnitude of ρ_{20}^{mol} is significantly reduced at 193 nm compared to the values obtained at longer wavelengths. The $K=4$ moments obtained at 193 nm are also dominated by a single term, that for ρ_{40}^{mol}.

The molecular frame moments can be used to construct both the angular momentum distribution of **L** (Refs. 40 and 41) and the electron density (or in this case the electron hole) distribution of the atomic oxygen.[12] Explicitly, the expression employed for the quantum mechanical angular momentum distribution[40,41] is

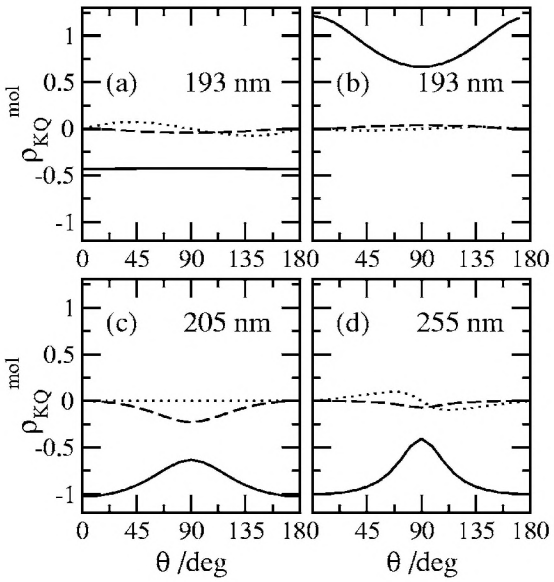

FIG. 6. The experimentally derived, scattering angle dependent molecular frame $\langle \rho_{KQ} \rangle$ moments obtained at [(a) and (b)] 193 nm, (c) 205 nm, and (d) 255 nm, the latter being taken from the data of Dylewski *et al.* (Ref. 22). The 193 nm data refer to moments of rank (a) $K=2$ and (b) $K=4$, while the data shown for longer wavelengths in (c) and (d) are for $K=2$ moments only. The symbols represent moments with $Q=0$ (—), $Q=1$ (···), and $Q=2$ (---).

$$Q(\theta_L,\phi_L)=\sum_{KQ}\frac{[K]}{4\pi}a_Q^{(K)}\langle LL,K0|LL\rangle C_{KQ}^{\ddagger}(\theta_L,\phi_L), \tag{9}$$

where the $a_Q^{(K)}$ polarization parameters of Refs. 40 and 41 are equivalent to $\rho_{KQ}^{\mathrm{mol}}/[K]^{1/2}$ used here. $\langle LL,K0|LL\rangle$ represents a Clebsch-Gordan coefficient, and the angles (θ_L,ϕ_L) define the direction of the minimum uncertainty state[40,41] in the molecular frame. To obtain information about the electron density distribution, we make use of the equation for the case of a two-electron atom,

$$N(\theta_e,\phi_e)=(-1)^{L+l}\frac{6[L]^{1/2}}{4\pi}\sum_{K,Q}\langle l0,l0|K0\rangle \times\begin{Bmatrix} L & L & K \\ l & l & l \end{Bmatrix} C_{KQ}(\theta_e,\phi_e)\rho_{KQ}^{\mathrm{mol}}, \tag{10}$$

which was derived in Appendix B of Ref. 12. Because $O(^1D_2)$ has a p^4 configuration, as opposed to p^2, the distribution worked out using Eq. (10) actually represents the unfilled orbital density or the electron hole distribution. Therefore, the angles (θ_e,ϕ_e) in Eq. (10) define the angular coordinates of the electron hole. The term in curly brackets in the same equation is a 6-J symbol. Note that unlike the L distribution, the Clebsch-Gordan coefficient appearing in Eq. (10) ensures that the electron hole distribution only contains even terms, with $K=0$ and 2.

The two distributions are shown in Fig. 7 for a recoil angle of 45° for photolysis wavelengths of 193, 205 and 255 nm, where the latter employs the alignment parameters of Dylewski *et al.*[22] Inspection of the molecular frame moments shown in Fig. 6 reveals that qualitatively similar results will be obtained at recoil angles other than 45°. As noted already, the derived distributions assume linearly polarized photolysis, although analogous plots can be constructed in the case of circularly polarized radiation. The L distribution obtained at 193 nm includes the small contribution arising from the orientation moment γ_1', leading to a small preference for orientation along the $-y$ direction. In confirmation of the above qualitative discussion, the angular momentum distributions [shown in the left-hand figures labeled (a)] peak perpendicular to the recoil direction, particularly so at longer wavelengths. Furthermore, in contrast to the L distributions, the corresponding electron hole distributions generated at 205 and 255 nm (Ref. 22) peak along the recoil axis $\pm z$. Thus, at these photolysis wavelengths, one may interpret the electron hole distribution as consisting primarily of the unfilled p orbitals lying along the recoil direction, i.e., two p_z holes. This is consistent with the L distribution, which suggests that the orbital angular momentum **L** together with the *filled* $p_{x,y}$ orbitals lie perpendicular to the recoil direction. This polarization implies that the recoiling $O(^1D_2)$ atoms are aligned in a Σ symmetry configuration, as discussed further in Sec. IV C. Note, finally, that whereas the electron hole distributions are quite strongly aligned along the z axis subsequent to excitation directly into the Hartley band, at 193 nm the distribution has more amplitude in the molecular frame xy plane, a point we return to in Sec. IV D.

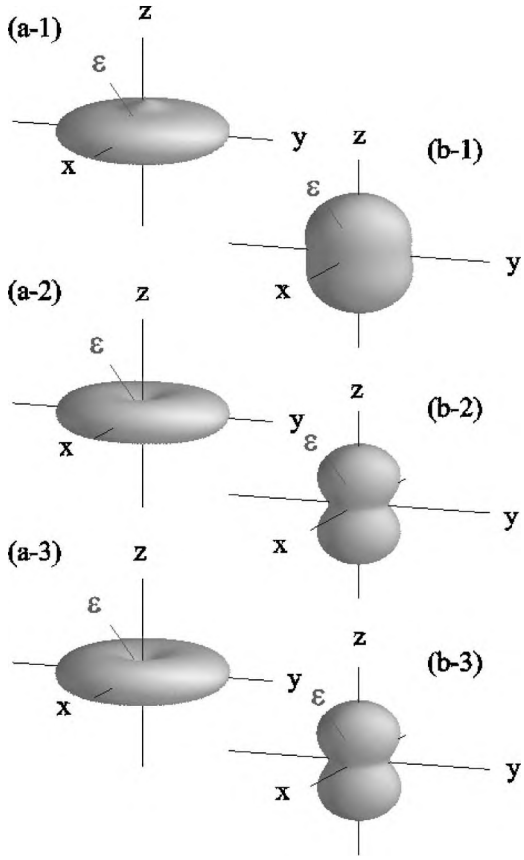

FIG. 7. The electronic orbital angular momentum [left (a)] and electron hole [right (b)] distributions obtained at (1) 193 nm, (2) 205 nm, and (3) 255 nm, the latter derived from the data of Dylewski (Ref. 22). All the results are for linearly polarized photolysis. Note that the 193 nm L distribution includes all nonzero moments up to and including $K=4$.

B. Long range potentials

In this section we follow the procedure employed to model polarization effects in the *singlet* channels of the pho-

todissociation of N_2O (Ref. 11) and NO_2.[14] We have also previously employed a similar treatment to calculate the polarization moments of $O(^3P)$ in the photofragmentation of N_2O and SO_2.[13] We restrict attention only to the channel generating $O(^1D_2)+O_2(a\ ^1\Delta_g)$ since this appears to be the channel that dominates and, in particular, has the most influence over the speed-integrated polarization parameters. It should be stressed at the outset that the model is an approximate one, intended to provide some insight about the interpretation of the polarization parameters measured here and elsewhere.[22,23,25] A quantitative analysis of these results would require a full quantum dynamical treatment of the photodissociation.

We start by defining a critical separation R_c in the exit channel and assuming the following.

- Before the critical separation R_c, the system evolves on some potential energy surface (the model does not say which one).
- The electronic wave function at this critical point is determined by first-order electrostatic interactions.
- After this point the fragments lose any contact and the wave function, transformed to the appropriate frame, determines the observed orbital angular momentum polarization of the oxygen atoms.
- Effects of coherent excitation of two surfaces are ignored.

In this section we take the molecular frame z axis to lie along the Jacobi coordinate R, with the diatomic molecule lying in the zx plane at some Jacobi angle γ. In Appendix C we give explicitly the γ dependence of interaction potential energy matrix $V^{\Lambda}_{MM'}$ in the long range region. This can be constructed in a basis $|\Lambda LM\rangle$, where $|\Lambda\rangle$ is the wave function for diatomic molecule A and $|LM\rangle$ is the electronic orbital wave function for atom B (here we rewrite M_L as M). We have assumed that the long range potentials are dominated by the quadrupole-quadrupole (Q-Q) interaction between $O(^1D_2)$ and $O_2(a\ ^1\Delta_g)$, and that, therefore, the choice of R_c becomes immaterial in the model. Because of the $1/R^5$ radial dependence of the Q-Q interaction, the latter will inevitably dominate at sufficiently large R. However, the quadrupole moment of $O_2(a\ ^1\Delta_g)$,[46] like that of ground state molecular oxygen,[47,48] is quite small, and it is possible that at the critical distance R_c, higher-order electrostatic terms or the dispersion interaction may play a more important role.[49,50] Note that only the anisotropic part of the dispersion interaction will have an effect on the atomic polarization predicted by the model. It is also worth mentioning that the atomic orbital polarization may be influenced by shorter range (anisotropic) exchange interactions. We emphasize that the present qualitative treatment does not take these additional interactions into account: These are points that would merit further consideration in future studies.[51]

Slices through the long range potential energy surfaces as a function of Jacobi angle are shown in Fig. 8. In the $D_{\infty h}$ point group, the $^1D_2$ state of atomic oxygen transforms as $\Sigma(M=0)$, $\Pi(M=\pm1)$, and $\Delta(M=\pm2)$. Therefore, as noted in Appendix C, combination of $O(^1D_2)$ with $O_2(^1\Delta_g)$ at linearity generates singlet molecular states of Σ^+, Σ^-, Π, Δ, Φ, and Γ symmetries. Note that at linearity the $^1\Delta$ molecular state of ozone arises from combination of $O_2(^1\Delta_g)$ with $O(^1D_2)$ atoms aligned with $M=0$. Within the present model, each of the five molecular ozone states shown in Fig. 8 is twofold degenerate (leading to ten molecular states in total), with pairs of A' and A'' levels reflecting the Λ-doublet levels of the $O_2(^1\Delta_g)$ coproduct, which in the model are treated as degenerate. Assignment of the ozone molecular states (see Table III) is achieved partly by inspection of the predicted orbital polarization (discussed below) and partly by reference to previous *ab initio* work.[42–44,52–55]. Note that for the A' states we use the diabatic notation employed by Hay *et al.*[52] A key feature for the discussion below is the assignment of the lowest energy ozone state to the Δ state at linearity, as opposed to the Σ/Γ pair of states. In the model this is determined by the signs of the quadrupole moments of $O_2(^1\Delta_g)$ and $O(^1D_2)$, and we have assumed that both of these are negative, consistent with theory.[14,46] Furthermore, the assignment also appears to be consistent with the *ab initio* calculations of Banichevich[53] and Peyerimhoff and Baloitcha and Balint-Kurti.[54] It is worth adding that the ordering of the states also coincides with that predicted on simple chemical grounds, in that one might expect the lowest molecular state of ozone to be formed when the unfilled p orbitals on O are aligned along the molecular axis of O_2, since this will involve minimum occupancy of the $O_2\sigma^*_u$ orbitals that will lie higher in energy than the corresponding π^*_g orbitals. While

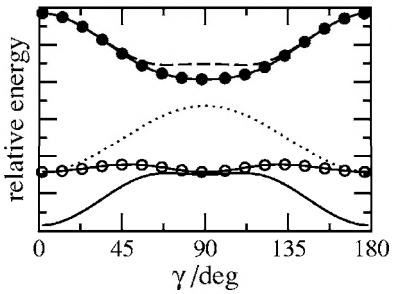

FIG. 8. Slices through the long range quadrupole-quadrupole potentials as a function of Jacobi angle γ. The notation employed is given in Table III. See text for details.

TABLE III. Assignment of the five doubly degenerate surfaces shown in Fig. 8. The C_{2v} assignments are the adiabatic correlations, which are probably secure for the A' states, which have been characterized recently using high level *ab initio* theory (Refs. 42–45), but are less clear for the A'' states. The "?" symbol indicates that assignment is unclear.

State	Symbol	$D_{\infty h}$ assignment	C_s assignment[a]	C_{2v} diabatic correlation
1	——	Δ	$3A'(\tilde{B})$ and $2A''$	$1\ ^1B_2$ and $1\ ^1A_2$
2	-○-○-○	Π/Φ	$4A'(\tilde{A})$ and $3A''$	$2\ ^1A_1$ and $2\ ^1A_2$
3	·-·-·	Φ/Π	$5A'(\tilde{C})$ and $4A''$	$2\ ^1B_2$ and $2\ ^1B_1$
4	-●-●-●-	Σ/Γ	$6A'(?)$ and A''	$3\ ^1A_1/4\ ^1A_1$ and ?
5	----	Γ/Σ	A' and A''	

[a]Labels of Hay *et al.* (Ref. 52) for the diabatic A' surfaces $(\tilde{A},\tilde{B},\tilde{C},\ldots)$ in parentheses.

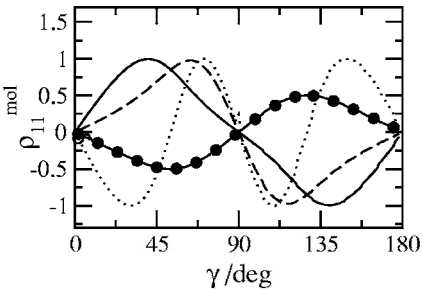

FIG. 9. The Jacobi angle dependence of that predicted $K=1$ orbital angular momentum moments calculated using the long range potentials shown in Fig. 8. The moments are labeled according to the states that give rise to them, with the same labeling as shown in Fig. 8 and Table III. Note that the moment for the state labeled (-○-○-○-) lies under that for the state labeled (-●-●-●-).

there is no reason for the quadrupole-quadrupole and chemical bonding interactions to yield the same energy ordering, that they appear to be the same is favorable for application of the model, because the correlation of the states from the short to the long range region is more straightforward. In assigning the remaining long range potential curves of ozone, we have made use of the available *ab initio* data.[42–44,52–55] The five lowest-lying singlet states of ozone of A' symmetry have been very accurately characterized in a number of recent studies,[42–44] and thus their assignment is more reliable than for the A'' states and the higher-lying A' and A'' states.

C. Polarization moments subsequent to excitation into the Hartley band

The eigenfunctions obtained from the above procedure can be used to obtain estimates for the multipole moments of the recoiling O atom via the equation,[5]

$$\rho_{KQ}(L) = \sum_{MM'} (-1)^{L-M} \langle LM, L-M' | KQ \rangle \rho_{MM'}(L),$$

with density matrix elements[13]

$$\rho_{MM'}(L) = c^*_{M'} c_M.$$

Here c_M are the expansion coefficients of the wave function for the electronic state of interest. As for ρ^{mol}_{KQ} (see Appendix B) we have renormalized the $\rho_{KQ}(L)$ moments such that $\rho_{00}(L)$ is unity. In the following we have assumed that the critical point R_c is at sufficiently large R that it can safely be taken to lie along the recoil direction. Hence we have not transformed the $\rho_{MM'}(L)$ into the molecular frame used in the experiments, which is defined with z along the recoil direction. The calculated polarization moments to be presented below depend on the Jacobi angle γ. It should be born in mind in the following discussion that a rigorous comparison between the calculated and experimental moments would require a full dynamical calculation, with the averaging over Jacobi angle taken into account explicitly.

The calculated moments are presented in Figs. 9 (for $K=1$) and 10 (for $K=2$ and 4). The orientation data shown in Fig. 9 may be compared with the experimentally derived molecular frame moment obtained at 193 nm displayed in Fig. 5(b). The calculated alignment moments can similarly be compared with the experimentally derived moments either obtained in the present work at 205 nm or with those measured previously by Dylewski *et al.* at 255 nm,[22] both of which are shown in Fig. 6. We start by considering this $K=2$ polarization data obtained subsequent to excitation into the Hartley band, at 205 and 255 nm.[22] The experimental polarization moments, and the electron hole and angular momentum distributions derived from them, reveal that $O(^1D_2)$ is formed in a state with preferential population of low M_L states (see Fig. 7), corresponding to an O-atom term of Σ symmetry at linearity. Therefore, as noted above, combination with the $O_2(^1\Delta_g)$ term would generate an ozone molecular state of $^1\Delta$ character at linearity. Recall that the experimental molecular frame moments are dominated by a large negative value for ρ^{mol}_{20}, particularly for recoil angles close to 0° and 180°. If we compare this result with the predicted moments shown in Fig. 10, it is clear that only two of the five pairs of states can account for such large negative ρ^{mol}_{20} moments, namely, the lowest Δ state [labeled (—) in the figure] at low Jacobi angles γ or the highest Σ/Γ state [labeled (---)] at Jacobi angles centered around 90°. The next significant feature of the experimental moments is that the ρ^{mol}_{22}, although small, is negative in sign, in agreement with the sign of the predicted ρ^{mol}_{22} moment for the state labeled Δ at linearity (—), but opposite in sign to that predicted for the

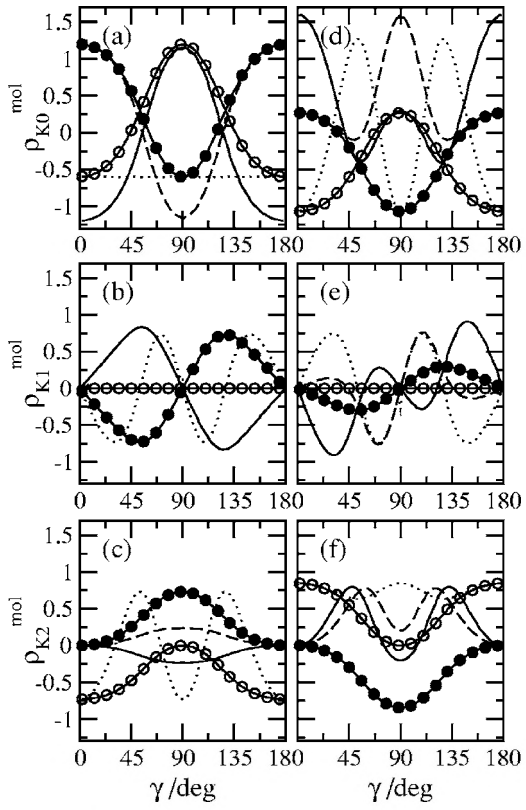

FIG. 10. The Jacobi angle dependence of that predicted $K=2$ [panels (a)–(c)] and $K=4$ [panels (d)–(f)] orbital angular momentum moments calculated using the long range potentials shown in Fig. 8. The moments are labeled according to the states that give rise to them, with the same labeling as shown in Fig. 8 and Table III. Note that the three rows of moments refer to data for $Q=0$, 1, and 2. In panel (b), the polarization moment for the state labeled (----) lies under that for the state labeled (——).

highest state labeled Σ/Γ (---) at linearity. Thus, comparison between the experimental and calculated polarization moments seems to point to dissociation on the lowest ozone molecular state, labeled Δ at linearity, and the preferential sampling of Jacobi angles γ less than $\sim 60°$. Although it is tempting to observe that the γ-angle dependence of the calculated moments appears to mimic the θ-angle dependence seen experimentally, it should be reemphasized that the dissociation will sample an undetermined range of γ angles that could only be quantified by means of a dynamical calculation. However, Jacobi angles $\leqslant 60°$ could be sampled preferentially, as suggested by the model, if ozone dissociated promptly at bond angles close to that of the ground state equilibrium geometry with little rotational excitation in the O_2 cofragment, which is perhaps not unreasonable for the fastest subset of $O(^1D_2)$ photofragments that tend to dominate the polarization measurements. Note that the lowest Δ symmetry state at linearity is precisely the one that is believed to correlate diabatically with the $\tilde{B}\,^1B_2(3\,^1A')$ state of ozone and is known to be responsible for the Hartley band,[42–45,52–54] as shown in Table III. The comparison between the calculated and observed polarization moments lends some support to the assignment of the electronic states in the long range region given in Table III and to the previously proposed (predominantly diabatic) dissociation mechanism subsequent to excitation into the Hartley band.[42–44]

D. 193 nm polarization data and possible dissociation mechanism

We now turn to the polarization data obtained at 193 nm. Because of the simplicity of the model, assignment of the participating electronic states solely on the grounds of the predicted angular momentum polarization moments would be unwise. In particular, the evidence presented above suggests that excitation at 193 nm may involve at least two electronic states, and under these circumstances coherence effects cannot, in general, be neglected. As noted in Sec. III, the negative translational anisotropy parameter obtained at this wavelength is consistent with excitation to states of either $^1B_1$ or $^1A_1$ symmetry. The high level *ab initio* calculations of Palmer and Nelson[55] suggest that excitation to either the $2\,^1B_1$ or $3\,^1A_1$ states dominates in this wavelength region, in good agreement with the present findings. Recall that some residual excitation into the $\tilde{B}(^1B_2)$ state, as at 205 nm, should also not be discounted. Added to this fact, the speed distribution obtained at 193 nm is consistent with the occurrence of dissociation into two product channels, correlating with O_2 born in either the $a\,^1\Delta_g$ or $b\,^1\Sigma_g^+$ electronic states.[17,20] Although a number of other excited states could well generate products in the same excited electronic states, the presence of the former channel, together with the similarity in the shape of the associated component of the speed distribution to that observed at longer wavelengths, provides some supporting evidence for residual excitation into the tail of the Hartley band. The production of $O_2(b\,^1\Sigma_g^+)$, on the other hand, could reflect excitation to a state that correlates with formation of these excited products. If these excited states were then crossed by states correlating with the lower $O(^1D_2)+O_2(^1\Delta_g)$ asymptote, this might account for the simultaneous production of O_2 in both its a and b electronic states. This behavior would be reminiscent of the crossing between the diabatic $\tilde{B}$ state, which gives rise to the Hartley band and is responsible for production of the $O(^1D_2)+O_2(^1\Delta_g)$, and the $\tilde{R}$ state, which leads to ground state atomic and molecular photofragments.[42,44,56]

The *ab initio* calculations of the $^1A'$ surfaces of Schinke and co-workers[44,45] and Baloitcha and Balint-Kurti[42,43] indicate the presence of a high-lying electronic state of ozone in the correct energy regime that appears to correlate with $O_2(b\,^1\Sigma_g^+)$ products. Unfortunately, these high-lying states have not been fully characterized by modern *ab initio* methods, so definitive assignment is difficult. Although we have not attempted a quantitative comparison between the model predictions and the experimental results, it would appear that weighted combinations of excitation into the Hartley band [labeled (—) in Figs. 8–10], together with the $2\,^1B_1$ (···) and/or $3\,^1A_1$ (–•–) states, might give plausible matches to the observed polarization data. It is interesting to note that the $2\,^1B_1$ and the $3\,^1A_1$ states are predicted to lead to $O(^1D_2)$ atoms with a preferential population of $M=\pm 1$ and ± 2 at linearity, as can be seen from the values of the calculated ρ_{20}^{mol} moments at $\gamma=0°$ and 180°, and this probably accounts for the increased probability in the electron hole distribution in the molecular frame xy plane, as was commented on at the end of Sec. IV A.

E. The $K=1$ orientation moments

As was mentioned in Sec. I B, an experimental study of the orientation of $O(^1D_2)$ subsequent to excitation into the Hartley band at wavelengths between 248 and 285 nm has recently been undertaken by Lee *et al.*[23] These experiments revealed a significant, speed-dependent γ_1' parameter, which on average is about a factor of 10 higher than we observe at 193 nm but is of the same sign. The newer work at 298 nm by Denzer *et al.*[25] yields a similar γ_1' parameter to those obtained by Lee *et al.*,[23] if the latter are averaged over recoil speed. Furthermore, once the γ_1' parameters are transformed into the molecular frame, they also agree well with the predicted orientation generated from the state of $^1\Delta$ symmetry at linearity that we have derived above from the long range model. In the present work at 193 nm, a much smaller value of γ_1' is obtained than was found subsequent to excitation at longer wavelengths into the Hartley band. However, as shown in Fig. 9, with the neglect of coherence effects, simultaneous excitation into the tail of the Hartley band and to either the $2\,^1B_1$ or the $3\,^1A_1$ states would be expected to generate small orientation, because the contributions to γ_1' from the two states are of opposite sign.

Interestingly, in the same experiments mentioned above, Lee *et al.*[23] found that the other two $K=1$ orientation parameters, α_1 and γ_1, corresponding to orientation along the z and x axes, respectively, were zero. For nonchiral systems, only orientation along the y axis is possible, while for chiral systems orientation along all three axes is possible.[6] For photofragment orientation to be observed along the z or x axis, the chirality in the products must be derived from the chirality of

the absorbed (circularly polarized) photon. Lee *et al.*[23] explained the zero values of α_1 and γ_1 by noting that, unlike the case in diatomics, for nonlinear polyatomic systems excited to a *single* potential energy surface, the photon helicity cannot be transferred to the products, because of the quenching of the orbital angular momentum on bending (thus Λ and Ω are no longer good quantum numbers). In the present work at 193 nm, we find that although all the orientation parameters are small, the γ_1 parameter is significantly larger than the γ_1' parameter. The question then arises as to whether or not, in contrast to the behavior observed at longer wavelengths, where excitation is believed to be to a single excited state,[23,25] the orientation generated at 193 nm could be a consequence of coherent excitation into two electronic states leading to the same asymptotic channel, namely, $O(^1D_2)+O_2(\Delta_g^1)$, as was suggested to be a possibility in Sec. IV D. This is an issue that needs to be investigated further in future theoretical studies.

V. CONCLUSIONS

The photodissociation dynamics of ozone at 193 nm has been studied using polarized laser photolysis coupled with velocity-map ion imaging. A comprehensive study of the $O(^1D_2)$ electronic orbital angular momentum polarization has been undertaken at this wavelength. Images obtained from dissociation at the probe laser wavelength of around 205 nm were also recorded and analyzed. The 205 nm polarization data were found to be in good agreement with previous studies by Dylewski *et al.*,[22] in which ozone was photolyzed close to the maximum in the Hartley band. Furthermore, the observed $O(^1D_2)$ speed distribution at 205 nm was found to be in excellent agreement with that calculated by Baloitcha and Balint-Kurti[42,43] for short wavelength dissociation of ozone via the $\tilde{B}\,^1B_2(3\,^1A')$ electronic state. The data reveal that at 205 nm, the dominant excitation and dissociation pathway is the same as it is for the Hartley band.

The experimental data set obtained at 193 nm shows a number of features that mark it out as different from that found at longer wavelengths. In agreement with previous work,[18,20] we find that the translational anisotropy has a different sign to that obtained subsequent to excitation into the Hartley band. The speed distribution of the $O(^1D_2)$ atoms also shows signs of bimodality, as observed previously in the molecular beam studies of Stranges *et al.*,[20] and is probably indicative of the production of O_2 in both the a and b electronic states. The angular momentum polarization data also confirm that different dissociation pathways are in operation compared with those at play subsequent to excitation into the Hartley band. Analysis of the long range potentials, along the lines previously employed to interpret polarization data from the photodissociation of N_2O Ref. 11 and SO_2,[13] is used to make predictions about the polarization that would be generated by dissociation on the states correlating with $O(^1D_2)+O_2(a\,^1\Delta_g)$ products. These calculations not only appear to confirm the mechanism proposed for the generation of these products via the Hartley band but also provide clues about which states are likely to be accessed in the long range region subsequent to photodissociation at 193 nm.

ACKNOWLEDGMENTS

The authors gratefully acknowledge the Royal Society for the award of Royal Society Fellowships to two of the authors (C.V. and G.A.D.R), the EPSRC for research grants, and NERC [for a studentship for anothor author (S.J.H)]. The authors gratefully acknowledge helpful discussions with Professor O. S. Vasyutinskii (Ioffe Institute, St. Petersburg) and Professor G. G. Balint-Kurti (Department of Physical and Theoretical Chemistry, Bristol University).

APPENDIX A: INTENSITY EXPRESSIONS

To obtain the integrated image intensity, we integrate the expression for the image over the image coordinates (r,Φ). The total image intensity can then be written as

$$\langle I^j\rangle = \Re\{\langle c_0^j\rangle\},$$

where

$$\langle c_0^j\rangle = \sum_{KQ} P_K\langle\rho_{KQ}\rangle C_{KQ}^*(\Theta_a^j,\Phi_a^j).$$

The integral of the moments can be written as

$$\langle\rho_{KQ}\rangle = 3\left(\frac{[K]}{[j_A]}\right)^{1/2}\sum_{qq'}(-1)^{K+Q+q}E_{KQ}(\mathbf{e}) \times[K]^{1/2}\langle f_K'(q,q';v)\rangle\begin{pmatrix}1 & 1 & K\\ q' & -q & -Q'\end{pmatrix} \times\begin{pmatrix}K & K & 0\\ -Q & Q & 0\end{pmatrix}\begin{pmatrix}K & K & 0\\ -Q' & Q' & 0\end{pmatrix}.$$

Substituting for the 3-J symbols and for $E_{KQ}(\mathbf{e})$ yields

$$\langle\rho_{KQ}\rangle = 3\left(\frac{[K]}{[j_A]}\right)^{1/2}\sum_{qq'}(-1)^{K+q'+s}\begin{pmatrix}1 & 1 & K\\ s & -s & 0\end{pmatrix} \times C_{KQ}(\Theta_d^j,\Phi_d^j)\langle f_K'(q,q';v)\rangle\begin{pmatrix}1 & 1 & K\\ q' & -q & -Q'\end{pmatrix},$$

which can be rewritten as

$$\langle\rho_{KQ}\rangle = \left(\frac{3[K]}{[j_A]}\right)^{1/2}(-1)^{K+s+1}\begin{pmatrix}1 & 1 & K\\ s & -s & 0\end{pmatrix}C_{KQ}(\Theta_d^j,\Phi_d^j)\langle A^K\rangle. \tag{A1}$$

Here $\langle A^K\rangle$ represents the total orientation or alignment and can be defined as

$$\langle A^K\rangle = \sum_{qq'}(-1)^{q'+1}\sqrt{3}\begin{pmatrix}1 & 1 & K\\ q' & -q & -Q'\end{pmatrix}\langle f_K'(q,q';v)\rangle. \tag{A2}$$

Note that the 3-J symbol in Eq. (A1) restricts the total alignment to moments $K\leqslant 2$ and for linearly polarized photolysis $(s=0)$ to even K only. Now substituting for Eq. (A1) into the expression for the image intensity and contracting the prod-

uct of spherical harmonics using the spherical harmonic addition theorem yield

$$\langle I^j\rangle = \Re\{\langle c_0^j\rangle\} = \sum_K P_K\left(\frac{3[K]}{[j_A]}\right)^{1/2}(-1)^{K+s+1} \times\begin{pmatrix}1 & 1 & K\\ s & -s & 0\end{pmatrix}\Re\{\langle A^K\rangle\}P_K(\cos\Theta_{da}), \tag{A3}$$

where Θ_{da} is the angle between the photolysis and analysis (probe) laser reference axes. This equation agrees with previous work, for example, Dixon,[1] from which it is clearly seen that the intensity depends only on the angle between the pump and probe axes. The expressions for the total polarization parameters $\langle A^K\rangle$ are

$$\langle A^0\rangle = 1,$$

$$\langle A^1\rangle = \sqrt{2}(\langle f_1'(1,1;v)\rangle + 2\Re\{\langle f_1'(1,0;v)\rangle\}) = \sqrt{\frac{2}{3}}V_1(j_A)(\sqrt{3}\alpha_1+\gamma_1),$$

$$\langle A^2\rangle = \sqrt{\frac{2}{5}}(\langle f_2'(1,1;v)\rangle - \langle f_2'(0,0;v)\rangle + 2\sqrt{3}\Re\{\langle f_2'(1,0;v)\rangle\} + \sqrt{6}\langle f_2'(1,-1;v)\rangle) = \sqrt{\frac{2}{5}}V_2(j_A)(\alpha_2+\gamma_2+\eta_2).$$

This last equation is in agreement with Bracker *et al.*,[4] apart from the slightly different normalization employed. In general, note that just two parameters determine the total intensity, $\langle A^1\rangle$ and $\langle A^2\rangle$. Terms involving the former parameter disappear for linearly polarized photolysis, as well as for all geometries with $\Theta_{da}=\pi/2$. An example of the latter is the counterpropagating geometry with linearly polarized photolysis and circularly polarized probe radiation.

APPENDIX B: MOLECULAR FRAME MOMENTS

The following describes how to obtain the molecular frame moments from the laboratory frame polarization parameters. The starting point is Eq. (16) of Bracker *et al.*:[4]

$$\rho_{KQ}(\Theta,\Phi;v) = \rho_{00}(\Theta,\Phi;v)\sum_{Q'} D^{K*}_{QQ'}(\Phi,\Theta,0)\rho^{\mathrm{mol}}_{KQ'}(\theta,\phi;v),$$

which can be inverted by premultiplying through by $D^K_{QQ''}(\phi,\theta,0)$ and summing over Q,

$$\sum_Q D^K_{QQ''}(\Phi,\Theta,0)\rho_{KQ}(\Theta,\Phi;v) = \rho_{00}(\Theta,\Phi;v)\sum_{QQ'} D^K_{QQ''}(\Phi,\Theta,0) \times D^{K*}_{QQ'}(\Phi,\Theta,0)\rho^{\mathrm{mol}}_{KQ'}(\theta,\phi;v).$$

Note that in the present work we have normalized $\rho^{\mathrm{mol}}_{00}(\theta,\phi;v)$ to unity. Using the sum rules for rotation matrices, this equation reduces to

$$\rho_{00}(\Theta,\Phi;v)\delta_{Q'Q''}\rho^{\mathrm{mol}}_{KQ'}(\theta,\phi;v) = \sum_Q D^K_{QQ''}(\Phi,\Theta,0)\rho_{KQ}(\Theta,\Phi;v),$$

which can be rewritten as

$$\rho^{\mathrm{mol}}_{KQ}(\theta,\phi;v) = \sum_{Q''} D^K_{Q''Q}(\Phi,\Theta,0)\frac{\rho_{KQ''}(\Theta,\Phi;v)}{\rho_{00}(\Theta,\Phi;v)}. \tag{B1}$$

The next step is to substitute for the laboratory frame moments using Eq. (2), using the sum rules again to contract the product of rotation matrices. We can then write

$$\rho^{\mathrm{mol}}_{KQ}(\theta,\phi;v) = \frac{3}{4\pi}\left(\frac{[K]}{[j_A]}\right)^{1/2}\frac{1}{\rho_{00}(\Theta,\Phi;v)} \times\sum_{k_d q_d}\sum_{qq'}(-1)^{K+q'}E_{k_d q_d}(\mathbf{e}) \times[k_d]^{1/2}f_K'(q,q';v) \times\begin{pmatrix}1 & 1 & k_d\\ q' & -q & -Q\end{pmatrix}D^{k_d}_{q_d Q}(\Phi,\Theta,0). \tag{B2}$$

We now need to turn to the equation for the dissociation light polarization tensor, $E_{k_d q_d}(\mathbf{e})$. In the molecular frame, the angles (θ,ϕ) define the direction of the electric vector of the photolysis light, not the direction of the laboratory frame Z axis. To achieve this, we need to set the angles (Θ_d^j,Φ_d^j) appearing in $E_{k_d q_d}(\mathbf{e})$ equal to zero, such that the laboratory frame Z axis and the direction of the electric vector of the photolysis light are coincident. With this identity, the laboratory angles (Θ,Φ) become coincident with the molecular frame angles (θ,ϕ),

$$E_{k_d q_d}(\mathbf{e}_j) = (-1)^s[k_d]^{1/2}\begin{pmatrix}1 & 1 & k_d\\ s & -s & 0\end{pmatrix}C_{k_d q_d}(0,0) = (-1)^s[k_d]^{1/2}\begin{pmatrix}1 & 1 & k_d\\ s & -s & 0\end{pmatrix}\delta_{q_d 0}.$$

On substitution into Eq. (B2) the resulting expression reduces to

$$\rho^{\mathrm{mol}}_{KQ}(\theta,\phi;v) = \frac{3}{4\pi}\left(\frac{[K]}{[j_A]}\right)^{1/2}\frac{1}{\rho_{00}(\theta,\phi;v)} \times\sum_{k_d}\sum_{qq'}(-1)^{K+q+s}[k_d]f_K'(q,q';v)\begin{pmatrix}1 & 1 & k_d\\ s & -s & 0\end{pmatrix} \times\begin{pmatrix}1 & 1 & k_d\\ q' & -q & -Q\end{pmatrix}C_{k_d Q}(\theta,0). \tag{B3}$$

Note that in this equation $Q=q'-q$ and that

$$\rho_{00}(\theta,\phi;v) = \frac{W(v)}{4\pi[j_A]^{1/2}}[1+\beta(v)P_2(\cos\theta)],$$

with

$$W(v) = \frac{f_0(0,0;v) + 2f_0(1,1;v)}{\langle f_0(0,0;v)\rangle + 2\langle f_0(1,1;v)\rangle}$$

and

$$\beta(v) = \frac{2[f_0(0,0;v) - f_0(1,1;v)]}{f_0(0,0;v) + 2f_0(1,1;v)}.$$

APPENDIX C: LONG RANGE POTENTIALS

In this section we take the molecular frame z axis to lie along the Jacobi coordinate R, with the diatomic molecule lying in the zx plane. In the following we give explicitly the interaction potential energy matrix V^{Λ}_{MM} in the long range region. This can be constructed in a basis $|\Lambda LM\rangle$, where $|\Lambda\rangle$ is the wave function for diatomic molecule A and $|LM\rangle$ is the electronic orbital wave function for atom B (here we rewrite M_L as M).

The multipole expansion of the Coulomb interaction between the diatomic molecule (A) and the atom (B) is given by[57]

$$\hat{V} = \sum_{l_A,l_B} R^{-(l_A+l_B+1)} \sum_{m_A,m_B} (-1)^{l_B} \left[\frac{(2l_A+2l_B)!}{(2l_A)!(2l_B)!}\right]^{1/2} \times \langle l_A m_A l_B m_B | (l_A+l_B)0\rangle \hat{Q}^{\mathrm{MF}}_{l_A,m_A} \hat{Q}^{\mathrm{MF}}_{l_B,m_B}, \quad \text{(C1)}$$

where the multipole operators ($\hat{Q}^{\mathrm{MF}}$) are defined in the molecular frame (MF) defined above, and from now on we will drop the superscript MF notation.

The computation of the diatomic part involves a rotation to the diatomic frame (DF),

$$\langle \Lambda|\hat{Q}_{l_A,m_A}|\Lambda'\rangle = \sum_{m'} \langle \Lambda|\hat{Q}^{\mathrm{DF}}_{l_A,m'}|\Lambda'\rangle D^{l_A*}_{m_A,m'}(0,\gamma,0), \quad \text{(C2)}$$

where $D^{l_A*}_{m_A,m'}(0,\gamma,0)$ is a Wigner rotation matrix element and γ is the Jacobi angle. $\langle \Lambda|\hat{Q}^{\mathrm{DF}}_{l_A m'}|\Lambda'\rangle$ is the expectation value of the multipole moment operator of the diatomic molecule A. The matrix element is zero unless $\Lambda = m' + \Lambda'$. Given that Λ and Λ' only take the values ± 2, m' is restricted to 0 or 4. Thus the quadrupole term $l_A = 2$ term must be diagonal in Λ, and Eq. (C2) reduces to

$$\begin{aligned}\langle 2|\hat{Q}_{l_A,m_A}|2\rangle &= \langle -2|\hat{Q}_{l_A,m_A}|-2\rangle \\ &= \langle \Lambda|\hat{Q}^{\mathrm{DF}}_{l_A,0}|\Lambda'\rangle D^{l_A*}_{m_A,0}(0,\gamma,0) \\ &= \langle \Lambda|\hat{Q}^{\mathrm{DF}}_{l_A,0}|\Lambda'\rangle C_{l_A m_A}(\gamma,0). \end{aligned} \quad \text{(C3)}$$

The first equality in this equation arises due to the reflection symmetry of the molecular wave function. Note that the hexadecapole $l_A = 4$ term is the first to contain an off-diagonal term $\langle \Lambda|\hat{Q}^{\mathrm{DF}}_{4,4}|\Lambda'\rangle$, but even in this case, it is probably safe to assume that it is smaller than the diagonal $\langle \Lambda|\hat{Q}^{\mathrm{DF}}_{4,0}|\Lambda'\rangle$ term. In the following we will restrict ourselves to the quadrupole terms of the expansion only, and therefore off-diagonal terms in the potential matrix will be neglected.

To evaluate the atomic part of the matrix elements we use the Wigner-Eckart theorem:

$$\langle LM|\hat{Q}_{l_B,m_B}|LM'\rangle = (-1)^{L-M} \begin{pmatrix} L & l_B & L \\ -M & m_B & M \end{pmatrix} \langle L\|\hat{Q}^{(l_B)}\|L\rangle, \quad \text{(C4)}$$

where $\langle L\|\hat{Q}^{(l_B)}\|L\rangle$ is the reduced matrix element of the multipole moment operator for atom B. Coroiu *et al.*[14] have recently shown that for $O(^1D_2)$, only the $l_B = 2$ term is nonzero and is negative in sign. Finally, the expression for the potential matrix elements is obtained by converting the Clebsch-Gordan coefficient from Eq. (C1) into a 3-J symbol through

$$\begin{aligned}&\langle l_A m_A l_B m_B | (l_A+l_B)0\rangle \\ &= \delta_{m_A,-m_B}(-1)^{l_A-l_B}(2l_A+2l_B+1)^{1/2} \\ &\quad \times \begin{pmatrix} l_A & l_B & l_A+l_B \\ +m_A & -m_A & 0 \end{pmatrix}. \end{aligned} \quad \text{(C5)}$$

Thus, expressing the matrix $V^{\Lambda}_{MM'}$ in terms of a multipole expansion yields

$$\begin{aligned} V^{\Lambda}_{MM'}(\gamma) &= \langle \Lambda LM|\hat{V}(\gamma)|\Lambda LM'\rangle \\ &= \sum_{l_A,l_B} \frac{\langle \Lambda|\hat{Q}^{\mathrm{DF}}_{l_A 0}|\Lambda\rangle \langle L\|\hat{Q}^{(l_B)}\|L\rangle}{R^{l_A+l_B+1}} \\ &\quad \times (-1)^{l_A+L-M} \left[\frac{(2l_A+2l_B+1)!}{(2l_A)!(2l_B)!}\right]^{1/2} \\ &\quad \times \sum_{m_A} \begin{pmatrix} l_A & l_B & l_A+l_B \\ m_A & -m_A & 0 \end{pmatrix} \\ &\quad \times \begin{pmatrix} L & l_B & L \\ -M & -m_A & M' \end{pmatrix} C_{l_A m_A}(\gamma,0). \end{aligned} \quad \text{(C6)}$$

As noted above, only terms diagonal in Λ are considered here, which is strictly only valid for the quadrupole-quadrupole term in the potential. Therefore, in the present application, the sums over l_A and l_B disappear and $l_A = l_B = 2$. Diagonalization of the matrix V, for a given value of γ, yields the eigenvalues (i.e., the long range potential energy surfaces) and eigenfunctions (i.e., the electronic wave functions in the $|\Lambda LM\rangle$ basis). Note that in the present case, because V is diagonal in $\pm\Lambda$, the problem reduces to solving two identical 5×5 matrices, yielding five pairs of degenerate A' or A'' states. Group theory tells us that these states correspond to the Σ^+, Σ^-, Π, Δ, Φ, and Γ states at linearity. In this model, R_c is located at sufficiently long range that the degeneracy of these states is not lifted on bending.

[1] R. N. Dixon, J. Chem. Phys. **85**, 1866 (1986).
[2] L. A. D. Siebbeles, M. Glass-Maujean, O. S. Vasyutinskii, J. A. Beswick, and I. Roncero, J. Chem. Phys. **100**, 3610 (1994).
[3] T. P. Rakitzis and R. N. Zare, J. Chem. Phys. **110**, 3341 (1999).
[4] A. S. Bracker, E. R. Wouters, A. G. Suits, and O. S. Vasyutinskii, J. Chem. Phys. **110**, 6749 (1999).
[5] R. N. Zare, *Angular Momentum* (World Scientific, New York, 1988).
[6] K. Blum, *Density Matrix Theory and Applications*, 2nd ed. (Plenum, New York, 1996).
[7] G. G. Balint-Kurti, A. J. Orr-Ewing, J. A. Beswisk, A. Brown, and O. S. Vasyutinskii, J. Chem. Phys. **116**, 10760 (2002).
[8] M. C. G. N. van Vroonhoven and G. C. Groenenboom, J. Chem. Phys. **116**, 1965 (2002).
[9] A. Brown, G. G. Balint-Kurti, and O. S. Vasyutinskii, J. Phys. Chem. A

108, 7790 (2004).
[10] T. P. Rakitzis, S. A. Kandel, A. J. Alexander, Z. H. Kim, and R. N. Zare, Science **281**, 1346 (1998).
[11] J. M. Teule, G. C. Groenenboom, D. W. Neyer, D. W. Chandler, and M. H. M. Janssen, Chem. Phys. Lett. **320**, 177 (2000).
[12] M. Brouard, A. P. Clark, C. Vallance, and O. S. Vasyutinskii, J. Chem. Phys. **119**, 771 (2003).
[13] M. Brouard, R. Cireasa, A. P. Clark, T. J. Preston, C. Vallance, G. C. Groenenboom, and O. S. Vasyutinskii, J. Phys. Chem. A **108**, 7965 (2004).
[14] A. M. Coroiu, D. H. Parker, G. C. Groenenboom, J. Barr, I. T. Novalbos, and B. J. Whitaker, Eur. Phys. J. D **38**, 151 (2006).
[15] N. J. Mason, J. M. Gingell, J. A. Davies, H. Zhou, I. C. Walker, and M. R. F. Siggel, J. Phys. B **29**, 3075 (1996).
[16] R. Atkinson, D. L. Baulch, R. A. Cox, J. N. Crowley, R. F. Hampson, R. G. Hynes, M. E. Jenkin, M. J. Rossi, and J. Troe, Atmos. Chem. Phys. **4**, 1461 (2004).
[17] A. A. Turnipseed, G. L. Vaghijiani, T. Gierczak, J. E. Thompson, and A. R. Ravishankara, J. Chem. Phys. **95**, 3244 (1991).
[18] K. Takahashi, N. Taniguchi, Y. Matsumi, and M. Kawasaki, Chem. Phys. **231**, 171 (1998).
[19] S. Nishida, F. Taketani, K. Takahashi, and Y. Matsumi, J. Phys. Chem. A **108**, 2710 (2004).
[20] D. Stranges, X. Yang, J. D. Chesko, and A. G. Suits, J. Chem. Phys. **102**, 6067 (1995).
[21] K. Takahashi, T. Nakayama, and Y. Matsumi, J. Phys. Chem. A **107**, 9368 (2003).
[22] S. M. Dylewski, J. D. Geiser, and P. L. Houston, J. Chem. Phys. **115**, 7460 (2001).
[23] S. K. Lee, D. Townsend, O. S. Vasyutinskii, and A. G. Suits, Phys. Chem. Chem. Phys. **7**, 1650 (2005).
[24] G. Hancock, S. J. Horrocks, P. J. Pearson, G. A. D. Ritchie, and D. F. Tibbetts, J. Chem. Phys. **122**, 244321 (2005).
[25] W. Denzer, S. J. Horrocks, P. J. Pearson, and G. A. D. Ritchie, Phys. Chem. Chem. Phys. **8**, 1 (2006).
[26] A. T. J. B. Eppink and D. H. Parker, Rev. Sci. Instrum. **68**, 3477 (1997).
[27] D. W. Chandler and P. L. Houston, J. Chem. Phys. **87**, 1445 (1987).
[28] M. Bass, M. Brouard, A. P. Clark, and C. Vallance, J. Chem. Phys. **117**, 8723 (2002).
[29] M. J. Bass, M. Brouard, A. P. Clark, B. Martínez-Haya, and C. Vallance, Phys. Chem. Chem. Phys. **5**, 856 (2003).
[30] B. Martínez-Haya, M. J. Bass, M. Brouard, C. Vallance, I. Torres, and J. Barr, J. Chem. Phys. **120**, 11042 (2004).
[31] NIST Atomic Spectra Database, Version 3, 2005, http://physics.nist.gov/PhysRefData/ASD/index.html
[32] B. Y. Chang, R. C. Hoetzlein, J. A. Mueller, J. D. Geiser, and P. L. Houston, Rev. Sci. Instrum. **69**, 1665 (1998).
[33] B. Buijsse, W. J. van der Zande, A. T. J. B. Eppink, D. H. Parker, B. R. Lewis, and S. T. Gibson, J. Chem. Phys. **108**, 7229 (1998).
[34] M. Ahmed, D. S. Peterka, A. S. Bracker, O. S. Vasyutinskii, and A. G. Suits, J. Chem. Phys. **110**, 4115 (1999).
[35] A. G. Smolin, O. S. Vasyutinskii, E. R. Wouters, and A. G. Suits, J. Chem. Phys. **121**, 6759 (2004).
[36] Y. Mo and T. Suzuki, J. Chem. Phys. **109**, 4691 (1998).
[37] D. V. Kupriyanov and O. S. Vasyutinskii, Chem. Phys. **171**, 25 (1993).
[38] B. V. Picheyev, A. G. Smolin, and O. S. Vasyutinskii, J. Phys. Chem. **101**, 7614 (1997).
[39] A. J. Alexander, J. Chem. Phys. **118**, 6234 (2003).
[40] M. P. de Miranda and F. J. Aoiz, Phys. Rev. Lett. **93**, 083201 (2004).
[41] M. P. de Miranda, F. J. Aoiz, V. Saez-Rabanos, and M. Brouard, J. Chem. Phys. **121**, 9830 (2004).
[42] E. Baloitcha and G. G. Balint-Kurti, J. Chem. Phys. **123**, 014306 (2005).
[43] E. Baloitcha and G. G. Balint-Kurti, Phys. Chem. Chem. Phys. **7**, 3829 (2005).
[44] Z.-W. Qu, H. Zhu, and R. Schinke, Chem. Phys. Lett. **377**, 359 (2003).
[45] Z.-W. Qu, H. Zhu, S. Y. Grebenshchikov, and R. Schinke, J. Chem. Phys. **123**, 074305 (2005).
[46] B. F. Minaev and V. A. Minaeva, Phys. Chem. Chem. Phys. **3**, 720 (2001).
[47] D. B. Lawson and J. F. Harrison, J. Phys. Chem. **101**, 4781 (1997).
[48] B. F. Minaev, Spectrochim. Acta, Part A **60**, 1027 (2004).
[49] L. F. Phillips, Chem. Phys. Lett. **169**, 253 (1990).
[50] T. D. Poulson, P. R. Ogilby, and K. V. Mikkelsen, J. Phys. Chem. A **102**, 8970 (1998).
[51] J. A. Beswick and O. S. Vasyutinskii, Comments At. Mol. Phys. **42**, 69 (1998).
[52] P. J. Hay, R. T. Pack, R. B. Walker, and E. J. Heller, J. Phys. Chem. **86**, 862 (1982).
[53] A. Banichevich and S. D. Peyerimhoff, Chem. Phys. **174**, 93 (1993).
[54] E. Baloitcha and G. G. Balint-Kurti, Chem. Phys. **178**, 155 (1993).
[55] M. H. Palmer and A. D. Nelson, Mol. Phys. **100**, 3601 (2002).
[56] Z.-W. Qu, H. Zhu, S. Y. Grebenshchikov, and R. Schinke, J. Chem. Phys. **122**, 191102 (2005).
[57] A. van der Avoird, P. E. S. Wormer, F. Mulder, and R. M. Berns, Top. Curr. Chem. **93**, 1 (1980).